Far-infrared electron-paramagnetic-resonance spectrometer utilizing a quasioptical reflection bridge

Keith A. Earle, Dmitriy S. Tipikin,[a] and Jack H. Freed
Baker Laboratory of Chemistry, Cornell University, Ithaca, New York 14853-1301

(Received 5 March 1996; accepted for publication 11 April 1996)

We describe a far-infrared electron-paramagnetic-resonance (EPR) spectrometer for broadband (100–300 GHz) use. The spectrometer is operated in the reflection mode and uses broadband quasioptical methods to separate the transmitted from the reflected radiation. We describe and illustrate its operation at 170 GHz (1.8 mm) and compare its performance to that of our transmission mode spectrometer operating at 250 GHz. We also discuss the advantages of the reflection bridge for performing EPR experiments over a broad range of frequencies, and we consider methods of improving the performance of the bridge. This includes a novel design for variable coupling of the reflection-mode Fabry–Pérot resonator. © *1996 American Institute of Physics.*
[S0034-6748(96)05507-4]

I. INTRODUCTION

Since its discovery in 1944 by Zavoisky, electron paramagnetic resonance (EPR) has typically been performed at frequencies lower than 40 GHz. This limitation is not a fundamental one; rather, it is a technical one. Recent developments in source, detector, and magnet technology have permitted the exploration of ever higher frequencies for EPR. These developments have been reviewed elsewhere.[1] High-frequency EPR, which we may take to be EPR performed at *W* band (95 GHz) and higher in frequency, is now well established,[2–4] following the pioneering work of Lebedev.[5]

Key advantages of high-field/high-frequency EPR are as follows: increased g-tensor resolution;[6] better resolution of the zero-field-splitting tensor;[7] and increased sensitivity to details of the rotational diffusion processes.[8] The majority of EPR spectroscopists exploring this new frequency regime uses microwave techniques to generate and detect the EPR signal. As the EPR frequency increases, however, conventional microwave propagation techniques become exceedingly lossy, and the usual components for constructing a microwave bridge (e.g., circulators, fundamental mode cavities, etc.) are unavailable above 150 GHz. Our group has introduced the use of modern quasioptical techniques[1,2] to overcome these difficulties at higher frequencies. One of the major advantages of quasioptical techniques is that they can be made broadband with very low insertion losses.[9] In their application to EPR, however, quasioptical techniques have hitherto been limited to transmission mode designs: either with a Fabry–Pérot (FP) resonator[1,2] or a single-pass transmission.[4]

The concept of a broadband, quasioptical spectrometer is also a natural consequence of developments in modern EPR where multifrequency studies have been used to elucidate details of structure and dynamics that are ambiguous from single-frequency studies.[6,10–12] In this article we report on a novel quasioptical reflection mode spectrometer that can be tuned to operate at any frequency between 100 and 300 GHz, and we study its performance at 170 GHz. Our reflection bridge is based on optical polarization coding techniques to separate the reflected EPR signal from the power incident on the FP resonator. This is the first implementation of a quasioptical reflection mode bridge for EPR. We discuss the design considerations for broadband operation in Appendix C, which develops the necessary quasioptical theory for understanding the principles of operation.

There are several advantages of reflection versus transmission mode spectroscopy. First of all, the reflection measurements can be performed in such a manner that the signal, which is typically small, can be observed on a low-power background. In transmission, an optimally coupled resonator will have a homodyne bias power equal to 1/4 of the available power from the source.[1] In other words, the small signal is riding on top of a high-power background, which can limit the dynamic range of the detector as we discuss in Ref. 1 and in Appendix A to this work. Theoretically, one expects an enhancement of S/N by a factor of about 15 from an optimally coupled reflection-mode bridge. In addition, a reflection-mode FP resonator provides better conversion of power into far-infrared (FIR) magnetic field (i.e., the coupling quality factor Q_C is improved[1]). Theoretically, one estimates a factor of 5 enhancement in S/N from better resonator coupling.[1] Also of some significance is the fact that a transmission spectrometer uses the entire length of the warm bore for the optical path, whereas a reflection bridge only uses (e.g., the lower) half for the optics, making the rest (e.g., the upper half) available for temperature control, resonator tuning arrangements, and other excitation sources (e.g., rf for electron-nuclear double resonance (ENDOR), or optical fibers for photoexcitation).

To optimize the performance of the reflection bridge we need a method of adjusting the coupling to the resonator in order to have a reflection null on resonance. The experimentally observable quantity is the loaded quality factor Q_L. It depends on the coupling to the cavity, i.e., Q_C, and the unloaded quality factor Q_U in the following way:[1,2]

$$\frac{1}{Q_L}=\frac{1}{Q_C}+\frac{1}{Q_U}. \tag{1}$$

[a]Permanent address: Institute of Chemical Physics of the Academy of Sciences of Russia, Ul. Kosygina 4, V-334 Moscow, Russia, GIS.

 0034-6748/96/67(7)/2502/12/$10.00

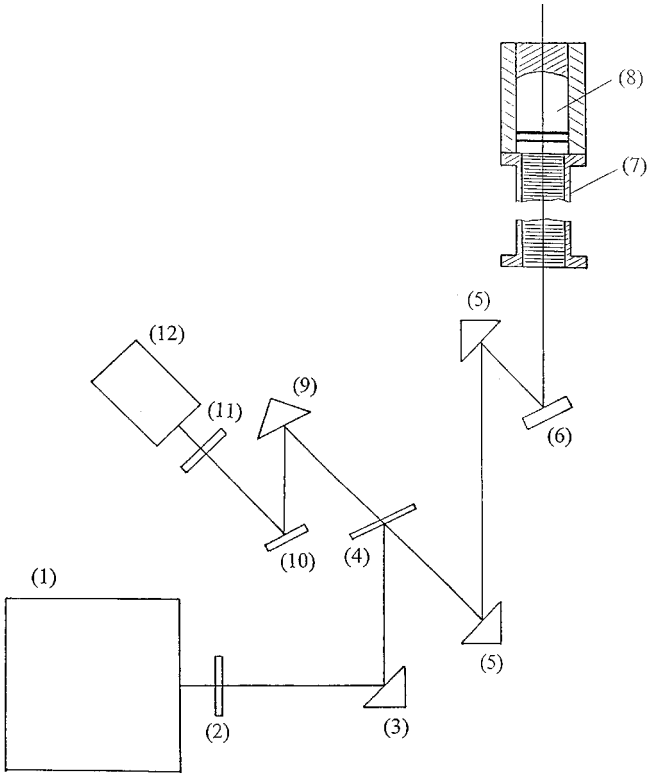

FIG. 1. Optical layout of the quasioptical reflection mode bridge. The components are numbered as follows: (1) source; (2) coupling lens; (3) paraboloidal focusing mirror; (4) duplexing grid; (5) Gaussian beam two-mirror telescope; (6) polarization transforming reflector; (7) corrugated waveguide; (8) mesh-coupled Fabry–Pérot resonator; (9) paraboloidal focusing mirror; (10) flat mirror; (11) focusing lens; and (12) detector.

For a reflection-mode spectrometer, it is well-known that one can achieve a reflection null on resonance when $Q_C = Q_U$. In this case, one may verify from Eq. (1) that $Q_L = Q_U/2$. The properties of the sample can have a profound effect on Q_U, independent of the coupling to the generator and detector. In this sense, we may say that the sample affects the unloaded quality factor Q_U of the resonator.

Our recent work with lipid dispersions[6] and conducting crown ether electrides[12] has emphasized the need for developing a means of variable coupling to the resonator. For such lossy samples, the unloaded quality factor of the resonator Q_U is much lower than Q_U for low-loss, simple fluids such as toluene.[8,11] In order to maintain a reflection null on resonance for such a variety of samples, it is necessary to vary Q_C so that the optimum $Q_L = Q_U/2$ can be maintained.

The drawbacks of conventional iris coupling for an open resonator such as a FP resonator are examined in detail by Matsui, Araki, and Kiyokawa.[13] We discuss a quasioptical variable coupling scheme below, which allows us to vary Q_C. It is discussed further elsewhere.[1]

In this article we discuss our initial success with the quasioptical bridge design. We describe the FIR-EPR spectrometer based on this bridge in Sec. II, and we discuss our tests and experiments in Sec. III.

II. SPECTROMETER

The optical layout of the spectrometer is shown in Fig. 1. The source (1) launches a linearly polarized Gaussian beam that is transformed to the appropriate beam waist radius by lens (2) and the first off-axis mirror (3). The beam waist radius is the $1/e$ radius of the Gaussian beam field amplitude at the position of least radial extent. Diffraction effects prevent the beam from being focused to a true point focus. For more details, the reader may consult the literature.[1,9] The beam waist radius is also called the beam waist for brevity. When we use the expression ''at the beam waist'' it refers to the plane normal to the optical axis which contains the circle defined by the beam waist radius.

After the beam waist has been transformed by lens (2) and off-axis mirror (3), the beam is reflected from the grid polarizer (4). The next two off-axis mirrors (5) form a Gaussian beam telescope, which focuses a converging beam onto the polarization transforming reflector (PTR) (6), which we configure as a quarter-wave plate.[14] Figure 2(a) shows the polarization evolution of the Gaussian beam as it propagates through the signal arm of the bridge. Figure 2(b) shows how the PTR accomplishes its polarization transformation function. We discuss the PTR in greater detail below. The beam waist at the output of the PTR is chosen to be at the aperture of the corrugated waveguide (7). We use corrugated waveguide for its low-loss, polarization-preserving properties, which we discuss in more detail below.

The PTR actually generates a circularly polarized beam as discussed below. This circularly polarized beam travels through the corrugated waveguide (7) and is incident on the resonator (8), which is shown in detail in Fig. 3. Due to the cylindrical symmetry of the resonator and the waveguide, a high degree of mode purity is maintained. As the external magnetic field is swept, the EPR absorption changes the unloaded quality factor Q_U. The loaded quality factor Q_L will therefore change according to Eq. (1). The coupling quality factor Q_C does not change, however. The EPR-induced violation of the condition $Q_C = Q_U$ changes the reflection coefficient of the resonator, and thus the level of the reflected signal. The reflected signal, still circularly polarized, travels through the corrugated waveguide (7) and retraverses the PTR (6), where it is converted back to a linearly polarized Gaussian beam orthogonal to the incident beam (see below). Thus, the PTR codes the EPR signal by polarizing it by $\pi/2$ with respect to the incident beam. Note that the PTR directs all of the incident beam to the resonator and all of the reflected signal to the detector, unlike a simple beam divider, which would discard half of the source power and half of the signal. Another virtue of the PTR for EPR is that in generating a circularly polarized beam from all of the incident radiation, the PTR increases the magnitude of the appropriate B_1 rotating field by a factor of $\sqrt{2}$ from what would be obtained with the original linearly polarized beam.

The returning beam is now transmitted through the grid polarizer (4) (i.e., the grid polarizer is precisely oriented to reflect a beam with the polarization of the incident beam, which guarantees that it will transmit a signal with polarization orthogonal to the original, reflected beam). The transmitted beam is focused onto the detector (12) by the final off-axis mirror (9), flat mirror (10), and lens (11). The flat mirror (10) is only used for convenience. We present a math-

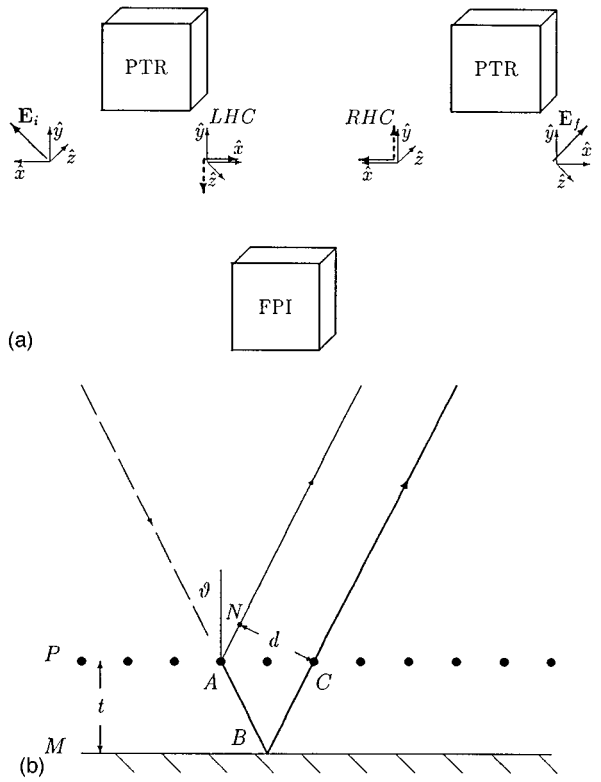

FIG. 2. (a) This figure shows the polarization evolution of a Gaussian beam as it traverses a polarization transforming reflector (PTR) and Fabry–Pérot interferometer (FPI) operating in reflection mode. Initially, the beam is linearly polarized at $+45°$. The exit beam is linearly polarized at $-45°$. The dotted lines indicate a polarization component that is retarded by a quarter period with respect to the polarization components indicated by a solid line. The optical layout shown here is an ''unfolded'' version of the polarization coding duplexer discussed in the section on reflection mode spectroscopy. We have unfolded the layout in order to indicate more clearly how the polarization develops. In the physical realization of this device, the FPI reflects the Gaussian beam back toward the PTR, the optical path retraces itself, and the exit beam propagates antiparallel to the initial beam with a final linear polarization rotated by $-90°$ with respect to the initial linear polarization. (b) This figure shows the optical path difference and the beam separation between the reflected and transmitted portions of a Gaussian beam incident on a polarization transforming reflector (PTR). The optical path difference $\Delta\mathscr{S}=AB+BC-AN$ is $2t\cos\vartheta$, where ϑ is the angle between the wave vector of the incident radiation and the normal to the plane of the PTR, and t is the separation between the grid polarizer P and the mirror M. The geometrical phase difference is $\varphi=k\Delta\mathscr{S}=4\pi t\cos\vartheta/\lambda$. We ignore contributions to φ from terms $\approx\Delta\mathscr{S}/z_0\ll 1$, where z_0 is the confocal distance. The beam separation is $d=2t\sin\vartheta$. The dashed line indicates radiation linearly polarized at an angle of 45° with respect to the page surface. The thin solid line indicates radiation linearly polarized in the plane of the page, and the thick solid line indicates radiation linearly polarized normal to the page.

ematical analysis of the PTR in Appendix B, which uses the Jones matrix formalism[15] to analyze the polarization state of the Gaussian beam upon passage through the PTR.

We now present a more in-depth discussion of four key components of the reflection bridge: the PTR, the corrugated waveguide, the reflecting optics, and the resonator.

A. The polarization transforming reflector (PTR)

A unique feature of the reflection bridge is the use of polarization coding[1] to separate, or duplex in engineering parlance, the transmitted and received Gaussian beams. Essentially, we use the grid polarizer (4) to separate the EPR signal from the excitation field. Radiation leaving the source is linearly polarized at 45° with respect to the normal to the plane of the page in Fig. 1. The EPR signal reflected back into the bridge is linearly polarized at $-45°$ after the PTR, as shown in Fig. 2(a), and can be separated for subsequent detection by the grid polarizer (4). It is for this reason that we use only those optical elements that preserve polarization.

The PTR performs its polarization transformation with a grid polarizer and a flat mirror to introduce a phase shift between two orthogonal components of a Gaussian beam. The mechanism for inducing the phase shift is shown in Fig. 2(b).

Suppose the PTR in Fig. 2(a) has its grid aligned vertically, i.e., along the y axis. In this orientation, half of the radiation will be transmitted and half of the radiation will be reflected, because the incident beam is polarized at 45° with respect to the vertical. At the output of the PTR, the output beam is circularly polarized by the appropriate choice of the

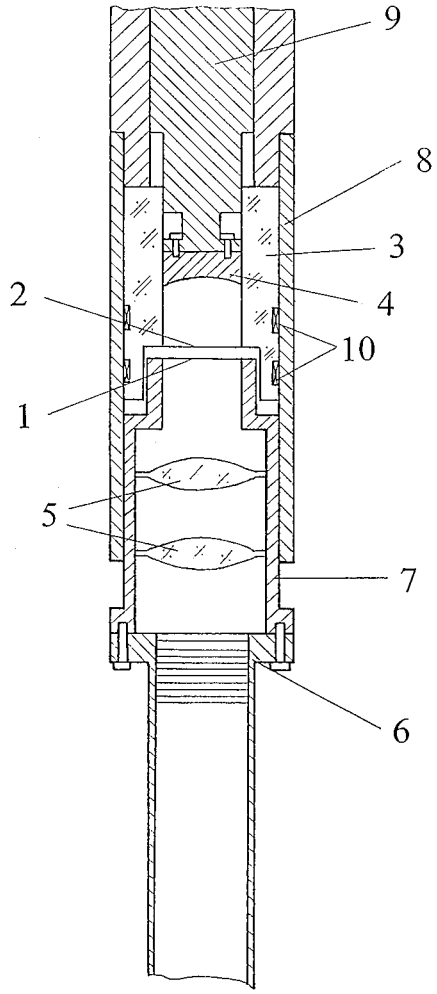

FIG. 3. Detailed optical layout of broadband Fabry–Pérot resonator. The components are numbered as follows: (1) external coupling mesh; (2) internal coupling mesh; (3) mirror guide sleeve; (4) spherical focusing mirror; (5) Gaussian beam coupling telescope; (6) corrugated waveguide; (7) external mesh tuning sleeve; (8) fixed resonator guide nut; (9) spherical mirror tuning rod; and (10) magnetic-field modulation coils. The components are discussed in detail in Sec. II.

grid mirror spacing [see Fig. 2(b) for a geometric construction of the path difference between the two components of the beam]. Upon reflection from the FP resonator [see Fig. 2(a)], the beam, still circularly polarized, is again analyzed into two orthogonal, linearly polarized components by the grid [see Fig. 2(b)]. The component transmitted by the grid has picked up a total phase shift of π with respect to the reflected component, which causes the output polarization to rotate by $\pi/2$ with respect to the initial polarization [see Fig. 2(a)].

The PTR is described in greater detail elsewhere[1,16] (see also Appendix B); it has many desirable features for this particular application. First of all, it is a low-loss device which can be tuned for use at any frequency from 100 to 300 GHz, by adjusting the grid/mirror spacing. Second, it has a high degree of mode purity when operated at a low angle of incidence and small beam displacement, as shown in Fig. 1 (see also Appendix B). It is also a compact device.

The mode purity of the PTR is an optimum at only one frequency for a given grid/mirror separation. For our application, this means that noise components outside of a narrow bandwidth centered on the carrier frequency will not be transmitted efficiently through the bridge. In particular, the noise components outside of the pass band of the PTR will be elliptically polarized, and only a portion of the noise power will be transmitted to the detector through the duplexing grid polarizer (4) in Fig. 1. Thus, the PTR functions as a tunable, noise-limiting, bandpass filter for the bridge. We have shown elsewhere[1] that the instantaneous bandwidth of the PTR is approximately $\nu_c/10$, where ν_c is the carrier frequency. At 170 GHz, the instantaneous bandwidth of the PTR is 17 GHz by this estimate, which provides a useful level of bandwidth limiting. Without a bandwidth-limiting component, the noise input characteristics are set by the input bandwidth of the waveguide in front of the Schottky diode, which can be 100 GHz or more in the FIR. We discuss the performance of the PTR in Sec. III.

B. Corrugated waveguide

For our initial experiments, we chose to use corrugated waveguide[17] with a bandwidth of approximately 3:1 (100–300 GHz), which puts our 170 GHz source at about midband. Unlike a conventional, smooth wall waveguide, a corrugated waveguide couples extremely efficiently to a Gaussian beam.[18] The cylindrical symmetry of the corrugated waveguide allows it to propagate circularly polarized beams with ease. The corrugations are necessary in order to make the wall of the waveguide reactive, which allows the balanced HE_{11} mode to propagate.[17] The pitch of the corrugations sets the high-frequency band edge. When the corrugation pitch equals 1/2 of the HE_{11} mode wavelength, Bragg scattering occurs, which distorts the Gaussian beam.[17] The diameter of the waveguide sets the low-frequency response. At sufficiently low frequencies, the attenuation becomes too large to be useful. Doane's article[17] should be consulted for a detailed comparison of the performance of smooth wall and corrugated waveguides.

C. Reflecting optics

We chose to use a combination of reflecting optics and corrugated waveguide for the broadband portion of the bridge. Metallic mirrors have two principal advantages over the lenses that we have used previously.[2] First of all, the reflectivity of most metals is essentially unity for the bandwidth of interest, 100–300 GHz, so that losses are not a problem. Second, metallic mirrors do not need the antireflection layers that are required for lenses in order for them to closely approach ideal performance, as we discuss below. In order to easily separate the incident beam from the reflected beam of a metallic mirror we use non-normal incidence, which limits our use of metallic mirrors to a region outside of the warm bore of the magnet, where there is enough room to position the optics in a sophisticated, nonlinear arrangement such as illustrated in Fig. 1.

In order to facilitate the manufacture of the reflecting optics, it is important to choose a diameter as small as is practical. Diffraction and beam truncation effects set a theoretical lower limit to the diameter of a lens or mirror in order to propagate undistorted Gaussian beams. An essentially pure Gaussian beam is preserved upon passage through an optical system if the aperture diameter is at least three times larger than the beam radius at the optical element.[15] The finite aperture converts some of the fundamental Gaussian beam into higher-order modes via diffraction effects, but the criterion we have stated corresponds to a mode conversion loss of -0.05 dB, which is negligible for most applications.[15] The longer the wavelength, the more stringent this criterion becomes. The aperture diameter is chosen to satisfy the low-loss propagation criterion for our lowest design frequency: 100 GHz.

The most useful mirror profiles for our system are concave ellipsoidal, which is analogous to a double convex lens, and concave paraboloidal, which is analogous to a plano-convex lens. We discuss the use of a concave spherical mirror at normal incidence in Sec. II D. When used at non-normal incidence, conic section mirrors have significant aberrations, but the aberrations can be cancelled if the mirrors are arranged appropriately in pairs.[19] The properties of such a Gaussian beam ''telescope'' are useful in a variety of applications.[9] We present a brief derivation of the properties of a Gaussian beam telescope in Appendix C.

By choosing the focal lengths of the paired reflecting optics appropriately, it is possible to make the input and output beam waist radii frequency independent,[9] which facilitates the design of a broadband bridge enormously. This point is particularly important for the coupling to the corrugated waveguide, which has a fixed input beam waist of 6.7 mm. If the input beam waist at the corrugated waveguide were frequency dependent, we would lose the desired broadband response.

There are three locations in the reflection bridge where the beam waist is on the order of the radiation wavelength: the output of the source; the input of the detector; and the input of the FP resonator. The source and detector couple to a small beam waist in order to make the coupling optics from free space to waveguide less bulky. The FP resonator (see

Sec. II D) uses a small beam waist to concentrate the FIR B_1 field in the resonator.

At these three places in the bridge, diffraction effects cause rapid beam growth because the beam waist is on the order of the radiation wavelength. For such small beam waists, it is difficult to couple the beam efficiently to a reflector at non-normal incidence. Optical elements at normal incidence couple symmetrically to a rapidly diverging beam and refocus it without introducing serious aberrations. For example, the spherical mirror in our FP resonator has the smallest focal length to aperture ratio of any element in the entire optical train. Yet, because it is used at normal incidence, we do not have to worry about beam aberrations.

At the output of the source and the input to the detector, we do not have the luxury of using reflecting optics at normal incidence, because we must separate the input from the output beam. The basic problem is that the aberrations inherent in a reflector with a small focal length to aperture ratio and non-normal incidence, which would otherwise couple efficiently to a beam with a small beam waist, quickly degrade the fundamental Gaussian content of the beam.[9,19] We discuss how one may use lenses to overcome these difficulties in Sec. II E.

D. Fabry–Pérot resonator

The resonator (8) in Fig. 1 is shown in more detail in Fig. 3. It is precisely located at the position of highest homogeneity in the warm bore of the 9 T magnet described previously.[2]

The meshes labeled (1) and (2) in Fig. 3 are used to vary the coupling into the resonator defined by the sleeve (3) and curved mirror (4). In order to understand how the meshes can vary the coupling into the resonator, we note the following useful optical equivalence theorem: Any multisurface optical system can be analyzed in terms of two equivalent surfaces.[20]

The two meshes (1) and (2) can thus be replaced by a fictitious equivalent surface whose apparent reflectivity may be varied by adjusting the spacing between meshes (1) and (2). This is the optical analog of a tuning screw in the iris of a conventional microwave cavity. We take the other optical surface to be the surface of the spherical mirror (4). These two surfaces, the fictitious equivalent surface and the physical surface of the curved mirror, define the dimensions of the resonator. The loaded quality factor Q_L and the reflected power is an involved function of the reflectivity of the meshes (1) and (2) and the spherical mirror (4) which we have derived in detail elsewhere.[1]

In order to compare the performance of this novel tuning arrangement with conventional methods of coupling, we also constructed an iris-coupled flat mirror which uses a conical horn to couple to the incident Gaussian beam, which we have used previously.[2] The coupling of this device is not variable, however. Nevertheless, we have found it to be a useful way to test the performance of the spectrometer as we discuss further in Sec. III.

We have also used the reflectivity of the sample itself to define the flat mirror of the resonator. This technique is useful for solid samples in special situations where the sample is thin enough so that it is not highly absorbing and yet has a sufficiently large conductivity so that it makes a good mirror. It is also necessary that the sample be flat and of sufficient radial extent so that it intercepts an appreciable fraction of the incident radiation.

The component that is common to all of the resonator configurations that we have studied is the spherical mirror. As we have discussed above, the Gaussian beam is focused down to a beam waist of approximately 2 mm on the sample. The role of the spherical mirror is to refocus the radiation onto the sample. In this sense it acts as a converging lens.

We should mention that there is a lower theoretical limit to the beam waist. In general, a free space Gaussian beam has a minimum beam radius of $w_0 > \lambda/2$ so that the approximations used to derive the Gaussian beam from Maxwell's equations will be valid.[1,9] Of course, the smaller the beam radius at the sample, the higher the FIR B_1 field, because the intensity, which is proportional to B_1^2, is higher. On the other hand, a small beam waist causes rapid beam growth, which requires a larger diameter spherical mirror to avoid beam truncation effects in the resonator. The argument is the same as given above in Sec. II C (see also the discussion in Lesurf[15]). A beam waist of 2 mm is a reasonable compromise between the desire for a large FIR B field at the sample and the necessity of limiting the radial extent of the spherical mirror.

The resonant frequencies of the resonator may be found by demanding that the beam in the resonator have a phase shift that is an integral multiple of π between the mirrors of the resonator. The beam growth in the resonator means that one cannot simply use plane wave analysis. Detailed calculations of the resonant frequency are available in the literature.[1,9,21] For our purposes, it is sufficient to note that the resonance condition corresponds approximately to a mirror/mesh separation that is an integral number of half-wavelengths.

We now wish to describe some of the more conventional elements of our reflection bridge spectrometer.

E. Coupling lenses

As we mentioned in Sec. II C, we use a small beam waist in the FP in order to concentrate the FIR B_1 field. A typical value is 2 mm, although it can be varied over a finite range to optimize the coupling to the EPR sample. The beam waist at the detector and source are on the same order, 1.7 mm, and as we also discussed in Sec. II C it is difficult to couple a small beam waist to a reflector at non-normal incidence.

For that reason we use lenses at the output of the source, input of the detector, and input to the FP resonator to transform the beam waist to a value that couples more easily to the bridge. Given that the sources and detectors in our current set up are optimized for a limited range, it is not a problem to manufacture lenses that are appropriate for each detector and source. The focal length is chosen so that the same physical position for the lenses can be used for all sources and detectors which facilitates multifrequency operation. We have also chosen the beam waist to be 1.7 mm for

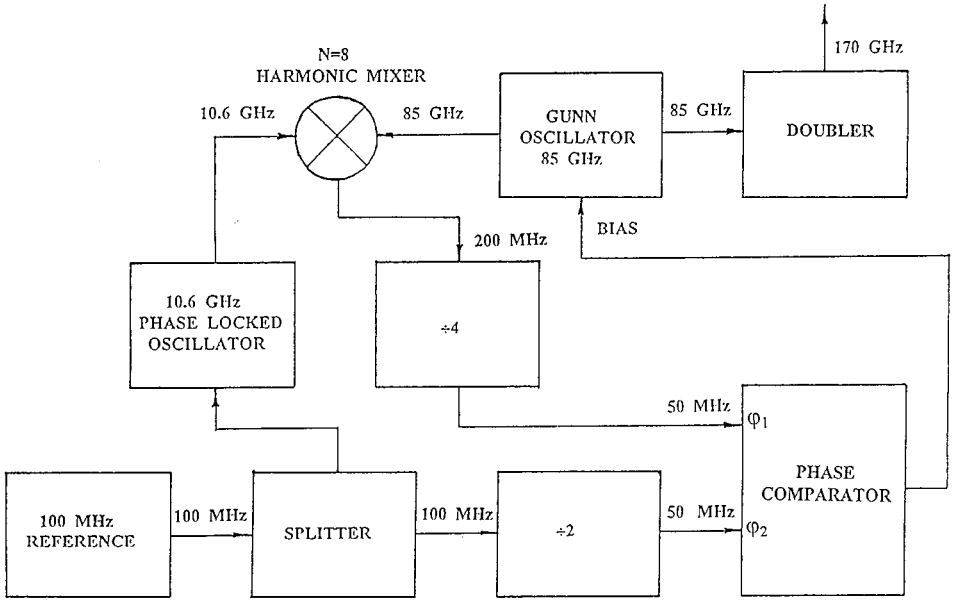

FIG. 4. Block diagram of phase-locked source at 170 GHz. The principles of operation are similar to classical frequency synthesizer designs.

all sources and detectors so that we can use a frequency-independent Gaussian beam telescope (see Appendix C) to couple into the bridge.

A two lens Gaussian telescope (5) in Fig. 3 (see also Appendix C) is used to couple the radiation from the output of the corrugated waveguide to the FP resonator. An axially symmetric system is desirable in the warm bore of the magnet because of space constraints, which is why we use two lenses to couple to the FP resonator as opposed to a mirror at non-normal incidence and a lens at the source and detector.

The property of lenses that makes them narrow band for our application is the necessity of providing antireflection grooves. The dielectric mismatch of a Teflon–air interface reflects ≈4% of the incident power unless some method is used to reduce the reflection. At 250 GHz,[2] we used Teflon lenses with antireflection grooves to reduce the reflection coefficient of the lens. The insertion loss of a lens with antireflection grooves is typically -0.15 dB.[15] We note that the dispersion and losses in Teflon are very low at these wavelengths.[22] Therefore, by using grooves of triangular cross section, it is possible to make an antireflection surface that is analogous to a tapered transmission line, with improved broadband performance.[23] For our initial experiments we used lenses optimized for 170 GHz.

All of the reflecting and refracting optics were machined at Cornell University using standard shop procedures[24] and standard machine shop tolerances. For the reflecting optics we note that the performance of an optical system in the FIR is diffraction limited, which means that reflecting optics must be machined to tolerances of at least $\lambda/20$ in order to approach diffraction-limited performance. Even at 300 GHz, which corresponds to a wavelength of 1 mm, $\lambda/20 \approx 0.002$ in. corresponding to a tolerance of ± 0.001 in., which is straightforward to accomplish with standard machine shop practices.

We have made a conscious effort to keep the number of lenses as low as possible in the reflection bridge because the antireflection grooves introduce a small astigmatic component in the beam which can degrade the purity of the Gaussian beam.[25] In practice, this is not a problem for the transmission mode spectrometer at 250 GHz,[2] even though it uses multiple lenses with antireflection grooves. Nevertheless, we have chosen a conservative approach for the reflection bridge that will limit this source of beam degradation.

F. Grid polarizers

We use grid polarizers in the reflection bridge for two purposes. First, we use them to discriminate between the polarization coded EPR signal and the excitation field, as we discussed in Sec. II A. Second, they are an important component of PTRs as we have shown in Sec. II A. We have measured the performance of our grid polarizers, and they provide a polarization discrimination of 30 dB, which is a useful level of performance. Our grid polarizers were purchased from Millitech Corporation, but the technology for making them is well known.[26]

G. Source

The source is similar to the unit used for measurements at 250 GHz. A block diagram of the source is shown in Fig. 4. The output of the doubler is connected to a TE_{01}–TE_{11} mode transducer,[27] which in turn connects to a Gaussian beam launching scalar feed horn.[18] In order to keep the scalar horn to a reasonable size, the output beam waist is chosen to be 1.7 mm. This is the same output beam waist that is used for the 250 GHz source and was chosen for compatibility with that device.

H. Diode detector

For these experiments we used a Millitech Schottky diode detector optimized for use over the 170–220 GHz band

with comparable performance to the unit used at 250 GHz.[2] The Schottky diodes are room-temperature devices that are easy to use. We have also used a broadband InSb hot-electron bolometer (Infrared Laboratories), which eliminates the need for switching detectors when operating in different bands. It is a cryogenic detector, however, which requires a regular schedule of maintenance.

I. Magnet

We now discuss how we use the EPR magnet designed for work at 250 GHz (8.9 T for $g=2.00$ systems) for our measurements at 170 GHz. At 170 GHz, the Larmor field is 6.05 T for $g=2.00$ systems. The mode of operation is quite similar to what we are accustomed to at 250 GHz;[2] namely, we charge the main coil to the desired field near the Larmor field and then use the sweep coils under the control of a programmable power supply in order to record a spectrum. The same power supplies that were used for the 250 GHz spectrometer were also used for these experiments. We use standard magnetic-field modulation at frequencies between 10 and 100 kHz in order to record first derivative spectra. The modulation coils are labeled (10) in Fig. 3. A Stanford programmable DSP lock-in is used to generate the reference signal for the magnetic field modulation and detection reference. The modulation signal is amplified by a home-built transconductance amplifier[6] tuned to the reference frequency.

J. Dewar

The Dewar that houses the magnet is different from the one we have used previously.[2] It has a longer hold time due to a larger He reservoir and more efficient design. Our previous hold time was 14 h. It is now 72 h, although we usually refill every 48 h in order to provide a safety margin. The warm bore diameter is 45.5 mm (1.790 in.) which is convenient for setting up experiments but does reduce the hold time over what is in principle achievable.

III. RESULTS

A. Bridge tuning

Our first experiments were designed to verify the principle of using the PTR to duplex the transmitted and received radiation. These experiments also allowed us to develop techniques for tuning the bridge for use at a given frequency.

In order to tune the bridge, we put a reflecting surface at the input of the corrugated waveguide so that all power that passes through the PTR is reflected back into the bridge. We used a beam chopper at 100 Hz to modulate the FIR source power. The source, a Millitech Corporation 10 mW phase-locked device, could damage the diode detector if all of the available power were incident on the diode. For the bridge tuning procedure, therefore, we attenuate the beam.

In our experience it is convenient to use a stack of cardboard sheets as an approximate variable attenuator. We have verified experimentally that the cardboard does not degrade the linear polarity of the Gaussian beam and, since a precise, repeatable value of attenuation is unimportant for this purpose, inhomogeneities in the cardboard which can cause variations in the attenuation from run to run are not a problem.

For precise values of attenuation, we use calibrated attenuators made from carbon black sandwiched between TPX (poly-methyl-pentene) layers similar to those described elsewhere.[2] These calibrated attenuators are primarily useful for varying the incident power on the resonator.

The duplexing grid (4) in Fig. 1 is initially oriented to reflect all power into the PTR (6). This is trivial to accomplish because the polarization of the source is known, and we can align the grid (4) by eye. We have also used the duplexing grid (4) as a continuously variable attenuator. The fraction of the power that is transmitted from the source to the PTR depends upon the orientation of the duplexing grid. The power incident on the PTR follows Malus's law $\propto\cos^2\vartheta$, where ϑ is the angular deviation of the grid orientation from the orientation that provides a reflection maximum.

In order to lower the standing wave ratio in the bridge, we put a beam dump behind the duplexing grid when operated as a variable attenuator. Note that the optical path in Fig. 1 allows us to separate the unused beam from the signal incident on the detector. In this sense, the duplexing grid uses spatial coding to multiplex the unused portion of the beam and the EPR signal. The well-defined, nonoverlapping Gaussian beams that we use are crucial to the success of this scheme.

Of course, if the duplexing grid (4) is rotated, the PTR (6) must be realigned to function properly. For this reason, we only use the duplexing grid (4) as a coarse attenuator.

The next step is to rotate the grid polarizer of the PTR (6), which is shown in more detail in Fig. 2(b), so that the PTR may produce a circularly polarized output beam, as discussed in Sec. II A and Appendix B. The spacing between the grid polarizer and the mirror of the PTR is now varied until there is a reflection maximum at the detector. Recall that for tuning purposes we reflect all of the power back into the bridge.

The orientation of the PTR grid and the spacing of the PTR mirror can now be optimized to find an absolute maximum in reflected power at the detector. This occurs at a grid/mirror separation such that the phase shift $\varphi=n\lambda/4$ where n is a small, odd integer. A large value of n corresponds to a large grid/mirror separation, which reduces the output beam overlap. This point is demonstrated graphically in Fig. 2(b).

In our current setup, there is a slight misalignment between the PTR grid and PTR mirror which limits the achievable overlap between transmitted and reflected beams (see the discussion by Earle and co-workers[1] and Appendix B). The consequence of the imperfect overlap is that there is incomplete conversion of linear to circular polarization on the first pass through the resonator and incomplete conversion of circular to linear polarization on the second pass. When the alignment is ideal, the polarization isolation should be 30 dB.[1] We have observed 17 dB with the current setup (a factor of 50), which is sufficient for demonstrating the principle. Whereas, we are taking steps to perfect the alignment of the PTR to obtain a level of performance comparable to

that reported in the literature,[16] our present purpose has been to demonstrate the feasibility of the EPR reflection bridge. We have also measured the polarization isolation via EPR. We return to this point after we discuss the performance of our resonator.

B. Resonator tuning

Once a reflection maximum has been found, the reflector at the input to the corrugated waveguide (7) in Fig. 1 may be removed and the resonator may be tuned. This is accomplished by varying the position of mirror (4) in Fig. 3 to find a reflection minimum on resonance and then varying the spacing between meshes (1) and (2) in Fig. 3, which varies the coupling into the resonator. If the resonator is critically coupled, the reflected power is zero on resonance. Once the resonator is tuned, we remove the chopper, sweep the magnetic field, and use standard magnetic-field modulation techniques to register the EPR signal.

The loaded Q of our resonator is rather low, $Q_L \approx 200$, which is comparable to the Q_L of our 250 GHz spectrometer, even though the coupling mechanism is quite different. The reflection minimum is also at a higher level than expected. We believe that the departure from the expected performance is due to two effects. First, the meshes must be mounted sufficiently flat[28] to minimize scattering and mode conversion losses. In addition, the coupling aperture at the input to the FP resonator is also known to play a crucial role in determining Q_L. The method of mounting the mesh must therefore ensure that the mesh is sufficiently flat and also that the coupling aperture diameter is optimized to minimize both the power lost to scattering in the resonator and the leakage power reflected on resonance.[13]

We are in the process of adapting mesh-mounting techniques that guarantee a high degree of flatness[29] to the confined geometry of our spectrometer. In addition, we are studying the optimum coupling aperture for minimizing scattering losses in the FP resonator.

In order to study the role of coupling in the performance of the FP resonator further, we replaced the meshes in the FP resonator with a conical horn that was coupled to a flat mirror via iris coupling. This arrangement is similar to one that we commonly use at 250 GHz.[2] We found that the resonances were comparable to what we have observed at 250 GHz. In fact, our first EPR spectrum from the 170 GHz bridge was taken on diphenylpicrylhydrazyl (DPPH) with the iris-coupled resonator. The spectrum of DPPH at 170 GHz is similar to what we observed at 250 GHz,[2] namely, it is a broad spectrum with evident polycrystalline structure.

C. Spectra of polyaniline

In order to proceed beyond simple tests and demonstrations of principle, we observed the EPR spectrum of polyaniline, a conducting polymer, prepared in the laboratory of Professor Khidekel at Chernogolovka.[30] The property of polyaniline that makes it intriguing for FIR-EPR studies is that there is significant exchange narrowing of the polyaniline FIR-EPR spectrum possibly mediated by polarons.[10] Spectra at 170 and 250 GHz were taken to elucidate the exchange-narrowing effect on the line shape. A detailed report of that research may be found elsewhere.[10] We discuss in Sec. III E how the 170 GHz spectra may be used to estimate the sensitivity of the 170 GHz spectrometer by comparison with the 250 GHz spectra.

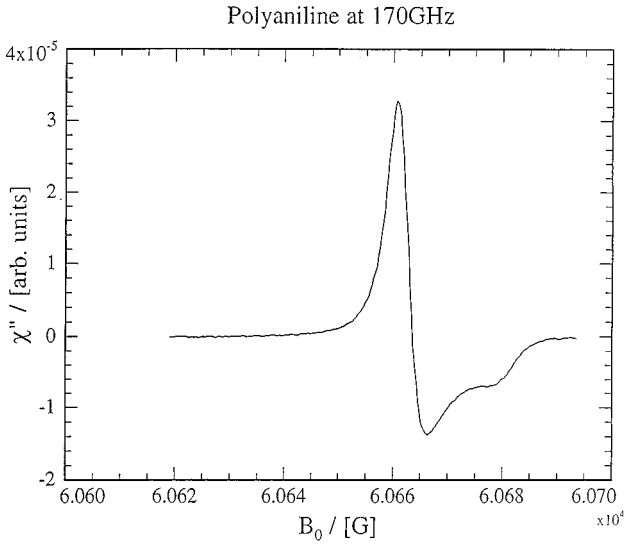

FIG. 5. EPR spectrum of polyaniline at 170 GHz. This spectrum was taken with a reflection bridge spectrometer. The signal-to-noise ratio is 530.

One feature of the experimental setup deserves further comment, however. The sample was prepared as a thin, round disk. We relied on the conductivity of the sample to define the bottom ''mirror'' of a low-Q FP resonator. We adjusted the power incident on the sample by tuning the position of the duplexing grid (4) in Fig. 1 to a suitable level as discussed above.

In order to avoid damaging the 170 GHz detector, we chose an incident power on the resonator of approximately 500 μW. Due to the low Q_L of this arrangement and the high reflectivity of the spherical mirror, much of this power was incident on the detector. We observed no deleterious effect from this level of incident power, except for a reduction in the dynamic range of the detector (see Appendix A).

The experimental spectrum at 170 GHz is shown in Fig. 5. Note that the signal to noise is excellent. In order to optimize the EPR signal once it is detected, we tune the position of the upper mirror (4) in Fig. 3 in order to maximize the FIR B_1 field at the sample with the field held constant.

D. EPR measurement of polarization isolation

There is an interesting feature of our bridge arrangement that we now discuss. Most EPR spectrometers use linearly polarized radiation at the sample, which may be considered to be a superposition of two counter-rotating, circularly polarized excitation fields. Only one of the circularly polarized components is effective at inducing EPR transitions, however.[31] Since we excite our sample with circularly polarized radiation, we need to ensure that we are generating the correct circularly polarized excitation field. Given that the correct choice of circular polarization state depends on the sign of the gyromagnetic ratio, then, in principle (if it were

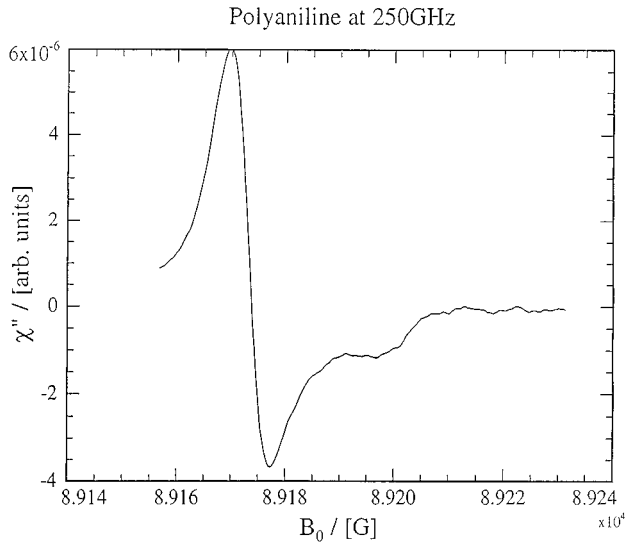

FIG. 6. EPR spectrum of polyaniline at 250 GHz. This spectrum was taken with a transmission mode spectrometer. The signal-to-noise ratio is 180.

not generally well known), our reflection bridge could be used to test the sign of the principal g-tensor values by measuring the signal strength of the EPR signal as a function of whether the incident radiation is right- or left-hand circularly polarized.

In order to test this feature of our spectrometer, we took 170 GHz EPR spectra of a polycrystalline DPPH sample in an iris-coupled resonator and varied the spacing between the grid and mirror of the PTR from $\lambda/4$ to $3\lambda/4$, etc. The polarization of the excitation field varies from left- to right-hand circularly polarized as the PTR is tuned to successive quarter-wave phase shifts. We observe that the EPR signal maximum does indeed vary between successive quarter-wave phase shifts of the PTR. The ratio between successive maxima is 13 dB, which allows us to infer that the degree of polarization isolation is also at that level. This level of polarization isolation is 4 dB less than the measurements made without the resonator (see the discussion in Sec. III A). We attribute the 4 dB difference to the coupling iris, which perturbs the Gaussian beam and reduces the mode purity of the beam.

E. Spectrometer sensitivity

In order to test the sensitivity of the 170 GHz spectrometer, we compared EPR spectra of the polyaniline sample we used for our measurements at 170 and 250 GHz. The 250 GHz spectrum is shown in Fig. 6. We estimate the signal to noise (S/N) for both spectra by comparing the low-field peak height to the rms noise voltage in the baseline. The signal to noise for the 170 GHz spectrum, shown in Fig. 5 is 530. The signal-to-noise ratio for the 250 GHz spectrum is 180. Based upon standard signal-to-noise considerations discussed by Earle and co-workers,[1] the fact that the same sample was used, and that many of the features of the spectrometer were the same or similar at the two frequencies, we are able to predict what the S/N should be, in principle. Our estimate [see Eq. (73) of Ref. 1] is that the S/N for the 170 GHz spectra should be about 40% that of the 250 GHz, instead of the observed factor of 3 greater S/N for the 170 GHz experiment. The standard analysis, however, does not take into account the extra virtues of a reflection bridge such as the weaker carrier signal reaching the detector, as noted in Sec. I. We are also aware of the subtle dependence of S/N on the precise location of a sample in the FP resonator.[32] Third, the insertion loss of the components for the reflection bridge is intrinsically lower than that for the transmission bridge (see the discussion in Secs. II C and II E). Lastly, we note that the reflection bridge is mechanically more rigid, because the components are mounted on a rigid base. It seems reasonable that these factors taken together could account for the better performance of the reflection bridge than a straightforward extension of the 250 GHz spectrometer performance would imply.

It is clear that improvement of the performance of the resonator would be the next key step in increasing the sensitivity of the 170 GHz bridge. This requires the full implementation of the double mesh coupling scheme of Sec. II D, which will enable us to match the FP resonator to further suppress any carrier signal from reaching the detector and will increase the resonator Q_L. In addition, by improving the alignment of the PTR to achieve maximum (i.e., 30 dB) polarization isolation, virtually all of the EPR signal will reach the detector. Since the PTR effectively acts as a low-Q bandpass filter (see the discussion in Sec. II A), such improved polarization isolation would also reduce the noise input to the detector.

In future work we also plan to address the broadband performance of this reflection-mode bridge.

ACKNOWLEDGMENTS

This work was supported by NIH Grant No. RR07126, and NSF Grant No. CHE9313167. The authors thank Professor P. F. Goldsmith and Professor D. E. Budil for many useful discussions. The meshes used in our initial experiments were a gift from Professor David E. Budil of the Northeastern University Chemistry Department.

APPENDIX A: EFFECT OF HIGH BACKGROUNDS ON SCHOTTKY DIODE DETECTORS

A large background power, which is an ineluctable consequence of the transmission mode, can dramatically reduce the sensitivity of diodes operated as detectors. The signal current I_S that flows in the detector is given by[33]

$$I_S = \beta P_{\mathrm{rf}}, \tag{A1}$$

$$\beta = \frac{e}{2nk_BT}\left(1+\frac{R_S}{R_B}\right)\left[1+\left(\frac{f}{f_C}\right)\right]^{-1}, \tag{A2}$$

$$R_B = \frac{nk_BT}{e(I_0+I_S)}, \tag{A3}$$

$$R_V = R_B + R_S, \tag{A4}$$

where P_{rf} is the power incident on the detector, β is the current responsivity of the diode, which is typically 1 μA/μW, e is the elementary charge of the electron, n is the

ideality factor of the diode, which is close to unity in a good design, k_B is the Boltzmann constant, T is the temperature of the diode, R_S is the spreading resistance of the diode, which is typically 5 Ω, R_B is the base-band dynamic resistance, which is typically 5000 Ω for incident powers up to a few μW, f is the frequency of the incident power, f_C is the cutoff frequency of the diode, which is approximately 1 THz for millimeter wave diodes, and I_0 is the dc bias current which is typically on the order of a few μA.

The figure of merit for a millimeter diode operated as a detector is the video resistance R_V, which in turn depends on R_B. R_B has a significant power dependence for high incident powers through its dependence on I_S. The current responsivity β is only weakly dependent on the incident power, and we will take it be 1 μA/μW for this analysis. For an incident power of 1 mW, Eq. (A1) implies $I_S=1$ mA, and we may use Eq. (A3) to show $R_B=25$ Ω. For an incident power of a few μW or lower, Eq. (A3) shows that R_B is essentially independent of input power and equal to 5000 Ω. Hence, high incident powers reduce the video resistance.

The minimum detectable signal for a detector is given by[33]

$$P_{\mathrm{rf,min}}=\frac{1}{\beta}\left(\frac{4k_BT\Delta f}{R_V}\right)^{1/2}, \tag{A5}$$

where Δf is the receiver bandwidth at the signal band, which is approximately 100 GHz for the WR-5 waveguide used in the fore-optics before the detector diode. Equation (A5) may be rewritten to estimate the ratio of minimum detectable powers for high and low background powers at the same receiver bandwidth

$$P^{\mathrm{Opt}}_{\mathrm{rf,min}}=P_{\mathrm{rf,min}}(25\ \ \Omega/5000\ \ \Omega)^{1/2},$$

which translates into a reduction of $P_{\mathrm{rf,min}}$ by 12 dB if we optimize the incident power on the detector.

For our transmission mode spectrometer at 250 GHz, we limit the incident power on the detector and thereby maintain its sensitivity. The most practical way to maintain high sensitivity without sacrificing source power is to work in the reflection mode. A well-matched resonator will have a reflected power of −30 dBc or lower, corresponding to background power levels of 1 μW or lower for a source power of 0 dBm (1 mW).

APPENDIX B: ANALYSIS OF THE POLARIZATION TRANSFORMING REFLECTOR

In order to proceed beyond a qualitative description of how a PTR operates, it is convenient to use a mathematical description of coherent polarization states, which are a good approximation to the output of solid-state near-millimeter sources. The Jones vector formalism is well known[14,15] and well suited to the present purpose. Any transverse polarization vector can be represented by an equation of the form $\mathbf{E}=(E_H\hat{H}+E_V\hat{V})$, where $\hat{H}$ and $\hat{V}$ are the basis vectors of horizontal and vertical polarization, respectively. Note that E_H and E_V may be complex, which is useful for describing circular polarization. In particular, $\mathbf{E}_{\pm}=E_0(\hat{H}\pm i\hat{V})$, where $+$indicates positive helicity and $-$indicates negative helicity.

A Jones vector is a matrix representation of **E**, viz.,

$$\mathbf{E}=\begin{bmatrix}E_V\\E_H\end{bmatrix}. \tag{B1}$$

The Jones vectors of a horizontally polarized Gaussian beam $\mathbf{E}_H$ and a vertically polarized Gaussian beam $\mathbf{E}_V$ of field strength E_0 at the beam waist may be represented as follows:

$$\mathbf{E}_V=E_0\begin{bmatrix}1\\0\end{bmatrix}e^{-\rho^2/w_0^2}, \tag{B2}$$

$$\mathbf{E}_H=E_0\begin{bmatrix}0\\1\end{bmatrix}e^{-\rho^2/w_0^2}, \tag{B3}$$

where w_0 is the beam waist radius. In terms of the coordinate system we have used above $|\mathbf{E}_V|=E_y$ and $|\mathbf{E}_H|=E_x$.

In Appendix C we use the system transfer matrix to study the effect of an optical system on the parameters of a Gaussian beam. A similar formalism exists for studying the polarization evolution of a Jones vector as a beam traverses a polarization transforming system. In this case the system transfer matrix is called a Jones matrix. The simplest Jones matrix is the matrix that describes the polarization vector reflected from an ideal mirror. In order to satisfy the boundary conditions of vanishing tangential E, we need a matrix with the following property:

$$\mathscr{M}\mathbf{E}=\begin{bmatrix}-E_V\\E_H\end{bmatrix}.$$

The following Jones matrix has the desired behavior:

$$\mathscr{M}=\begin{bmatrix}-1&0\\0&1\end{bmatrix}. \tag{B4}$$

A grid polarizer is the next object we need to consider. First we define the Jones vectors for linear polarization at ±45° with respect to the y axis. These cases correspond to the situation shown in Fig. 2(a). The required Jones vectors are

$$\mathbf{E}_{45}=\frac{E_0}{\sqrt{2}}\begin{pmatrix}1\\1\end{pmatrix},\quad \mathbf{E}_{-45}=\frac{E_0}{\sqrt{2}}\begin{pmatrix}-1\\1\end{pmatrix}.$$

A grid polarizer with the grid lines at a given angle φ with respect to the y axis will reflect radiation that is linearly polarized along the grid lines. If the grid lines make a ±45° with respect to the y axis, we need Jones matrices with the following behavior:

$$\mathscr{G}(45)E_{45}=-E_{-45},$$

$$\mathscr{G}(45)E_{-45}=0,$$

$$\mathscr{G}(-45)E_{45}=0,$$

$$\mathscr{G}(-45)E_{-45}=-E_{45}.$$

A Jones matrix that has this behavior is

$$\mathscr{G}(\pm 45)=\begin{pmatrix}-1/2&\mp 1/2\\ \pm 1/2&1/2\end{pmatrix}. \tag{B5}$$

We will not derive the form of $\mathscr{G}$ for an arbitrary inclination angle of the grid wires. One may verify that Eq. (B5) is a special case of the following general relation[15] for arbitrary grid orientation angle ϑ,

$$\mathscr{G}(\vartheta)=\begin{pmatrix} -\cos^2\vartheta & -\cos\vartheta\sin\vartheta \\ \cos\vartheta\sin\vartheta & \sin^2\vartheta \end{pmatrix}. \tag{B6}$$

It is important to note that the preferred orientation of the grid for non-normal incidence is with the grid in the plane of incidence of the Gaussian beam.[34] This corresponds to $\vartheta=90°$. For this orientation of the grid, nonidealities due to cross-polarized components are minimized. The field transmitted by the polarizer is described by the complement of the Jones matrix of the polarizer, viz., $\mathscr{G}_{\mathbf{T}}(\vartheta)$, which has the following functional form:[15]

$$\mathscr{G}_{\mathbf{T}}(\vartheta)=\begin{pmatrix} \sin^2\vartheta & -\cos\vartheta\sin\vartheta \\ -\cos\vartheta\sin\vartheta & \cos^2\vartheta \end{pmatrix}. \tag{B7}$$

The PTR shown in Fig. 2 can be analyzed along conventional lines.[16] In our notation, we may use the Jones matrices of a polarizer $\mathscr{G}$, its complement $\mathscr{G}_{\mathbf{T}}$, and a mirror $\mathscr{M}$ to write down an expression for the output beam of a PTR $\mathbf{E}_r$ at the grid surface (where we may choose the beam radius $w\approx w_0$), viz.,

$$\mathbf{E}_r=[\mathscr{G}(\vartheta)e^{-\rho^2/w_0^2}+\mathscr{M}\mathscr{G}_{\mathbf{T}}(\vartheta)e^{-i\varphi}e^{-(\boldsymbol{\rho}-\mathbf{d})^2/w_0^2}]\mathbf{E}_i, \tag{B8}$$

where $e^{-i\varphi}$ is a factor due to the phase shift of the transmitted portion of the incident beam, $\mathbf{E}_i$ is the Jones vector of the incident radiation,

$$\varphi=4\pi t\cos\vartheta/\lambda, \tag{B9}$$

where t is the separation of the grid and flat mirror and ϑ is the angle of incidence of the gaussian beam on the PTR, and $\mathbf{d}$ is the displacement vector of the transmitted beam along the x axis of the reflected beam whose magnitude is given by

$$d=2t\sin\vartheta. \tag{B10}$$

We explicitly include the exponential factors $\exp(-\rho^2/w_0^2)$ and $\exp[-(\boldsymbol{\rho}-\mathbf{d})^2/w_0^2]$ in order to display the effects of beam displacement on the performance of the PTR. The reader is referred elsewhere for details.[1] To summarize, the deviation of the practical device from the ideal response depends upon the ratio d/w_0. The nonidealities can be kept to power levels approximately 30 dB below the desired polarization, if w_0 is sufficiently large and ϑ is sufficiently small. For our purposes, $w_0=6.7$ mm and $\vartheta=22.5°$ approach this level of performance. We note a degradation in the PTR response from a slight misalignment of the grid and flat mirror. In the future, we shall shim the grid to improve the overlap of the two outputs of the PTR.

The ideal response of PTR, $\mathscr{P}(\vartheta,\varphi)$, in the absence of beam displacement effects, i.e., $w_0\to\infty$, may be written in Jones matrix form as follows:

$$\mathscr{P}(\vartheta,\varphi)=\mathscr{G}(\vartheta)+\mathscr{M}\mathscr{G}_{\mathbf{T}}(\vartheta)e^{-i\varphi}. \tag{B11}$$

The interested reader may use Eq. (B11) to analyze the response of the PTR to various initial polarization states. Figure 2 may be consulted to visualize the results of the analysis.

APPENDIX C: ANALYSIS OF THE GAUSSIAN BEAM TELESCOPE

One of the design goals for the reflection bridge spectrometer is to make it a broadband device. In order to do so, it is convenient to use the concept of the Gaussian beam telescope,[9] which transforms the beam waist of a given input beam $w_0^{(\mathrm{in})}$ to a beam described by a beam waist $w_0^{(\mathrm{out})}$. The great advantage of the Gaussian beam telescope is that the beam transformation is independent of frequency. In order to analyze the telescope, we will use the quasioptical equivalent of the ''ABCD'' law, formulated by Kogelnik,[21] which allows us to calculate the beam radius and radius of curvature of the equiphase front of the beam at the output of an optical train if the input beam radius and phase front radius of curvature are known. In the sequel we refer to the beam radius and radius of curvature. The radius of curvature refers to the radius of curvature of the equiphase surface, or phase front, of the beam. We hope this compact terminology will not cause confusion. From the context it should be clear what is meant.

Kogelnik[21] has shown that an arbitrary optical system may be described by a 2×2 system transfer matrix $\mathscr{M}$, which is the matrix product of 2×2 transfer matrices $\mathscr{M}_i$ for each element in the optical train. Furthermore, it is convenient to combine the radius of curvature and beam radius of the Gaussian beam into the so-called q parameter, viz.,

$$\frac{1}{q}=\frac{1}{R}-i\frac{\lambda}{\pi w^2}, \tag{C1}$$

where R is the radius of curvature, w is the beam radius, and λ is the radiation wavelength. For our purposes it is sufficient to consider a special class of q parameters. At the beam waist the radius of curvature is infinite and the q parameter is pure imaginary. For this special case, we may write

$$q_i=iz_0^{(i)}, \tag{C2}$$

where $z_0^{(i)}=\pi(w_0^{(i)})^2/\lambda$, the confocal parameter[1] for a beam of waist radius $w_0^{(i)}$. In the sequel, the index i will distinguish the input and output beam waists.

If the transfer matrix $\mathscr{M}$ is written in the form

$$\mathscr{M}=\begin{pmatrix} A & B \\ C & D \end{pmatrix}, \tag{C3}$$

then Kogelnik has shown[21] that the output q parameter may be found as follows:

$$q_{\mathrm{out}}=\frac{Aq_{\mathrm{in}}+B}{Cq_{\mathrm{in}}+D}. \tag{C4}$$

The transfer matrix for propagation through a distance d_i is

$$\mathscr{T}(d_i)=\begin{pmatrix} 1 & d_i \\ 0 & 1 \end{pmatrix}. \tag{C5}$$

The transfer matrix for a lens, or reflector, of focal length f_i is

$$\mathscr{L}(f_i)=\begin{pmatrix} 1 & 0 \\ -1/f_i & 1 \end{pmatrix}. \tag{C6}$$

We wish to calculate the transfer matrix for an optical system consisting of two ''lenses'' whether reflecting or refracting, separated by the sum of their focal lengths with a beam waist located at a distance f_1 away from the first lens. We then ask, what is the output beam q parameter at a distance f_2 from the second lens? Symbolically, we write

$$\mathscr{M}=\mathscr{T}(f_2)\mathscr{L}(f_2)\mathscr{T}(f_2+f_1)\mathscr{L}(f_1)\mathscr{T}(f_1) \tag{C7}$$

$$=\begin{pmatrix} -f_2/f_1 & 0 \\ 0 & -f_1/f_2 \end{pmatrix}, \tag{C8}$$

where we have used Eq. (C5) and (C6) to write Eq. (C8).

We may now use the ABCD law expressed by Eq. (C4), where the elements of the transfer matrix are given by Eq. (C8), to calculate the output beam q parameter, viz.,

$$q_{\text{out}}=\frac{f_2^2}{f_1^2}\,q_{\text{in}}. \tag{C9}$$

If the input beam has a beam waist of $w_0^{(\text{in})}$ at a distance f_1 from the first lens so that q_{in} is purely imaginary, then, using the fact that q_{out} in Eq. (C9) must be purely imaginary as well, we may infer that there is a beam waist in the output beam at a distance f_2 from the second lens. Explicitly,

$$w_0^{(\text{out})}=(f_2/f_1)w_0^{(\text{in})}, \tag{C10}$$

where we have used Eq. (C2). Note that the result in Eq. (C10) is independent of frequency, as we claimed.

[1] K. A. Earle, D. E. Budil, and J. H. Freed, in *Advances in Magnetic and Optical Resonance*, edited by W. Warren (Academic, New York, 1996), Vol. 19, Chap. 3.

[2] W. B. Lynch, K. A. Earle, and J. H. Freed, Rev. Sci. Instrum. **59**, 1345 (1988).

[3] J. A. Allgeier, J. A. J. M. Disselhorst, R. T. Weber, W. T. Wenckebach, and J. Schmidt, in *Modern Pulsed and Continuous Wave Electron Paramagnetic Resonance*, edited by L. Kevan and M. Bowman (Wiley, New York, 1990), Chap. 6.

[4] A. L. Barra, L.-C. Brunel, and J. B. Robert, Chem. Phys. Lett. **165**, 107 (1990).

[5] O. Y. Grinberg, A. A. Dubinskij, and Y. S. Lebedev, Russ. Chem. Rev. **52**, 850 (1983).

[6] K. A. Earle, J. K. Moscicki, M. Ge, D. E. Budil, and J. H. Freed, Biophys. J. **66**, 1213 (1994).

[7] W. B. Lynch, R. S. Boorse, and J. H. Freed, J. Am. Chem. Soc. **115**, 10 909 (1993).

[8] K. A. Earle, D. E. Budil, and J. H. Freed, J. Phys. Chem. **97**, 13 289 (1993).

[9] P. F. Goldsmith, in *Infrared and Millimeter Waves: Systems and Components*, edited by K. J. Button (Academic, New York, 1982), Chap. 5.

[10] D. S. Tipikin, K. A. Earle, and J. H. Freed (unpublished).

[11] D. E. Budil, K. A. Earle, and J. H. Freed, J. Phys. Chem. **97**, 1294 (1993).

[12] D. H. Shin, J. L. Dye, D. E. Budil, K. A. Earle, and J. H. Freed, J. Phys. Chem. **97**, 1213 (1993).

[13] T. Matsui, K. Araki, and M. Kiyokawa, IEEE Trans. Microwave Theory Tech. **MTT-41**, 1710 (1993).

[14] E. Hecht and A. Zajac, *Optics* (Addison–Wesley, Reading, MA, 1979).

[15] J. C. G. Lesurf, *Millimeter-wave optics, devices and systems* (Adam Hilger, London, 1990).

[16] J. Howard, W. A. Peebles, and N. C. Luhmann, Jr., Int. J. Infrared Millimeter Waves **7**, 1591 (1986).

[17] J. L. Doane, in *Millimeter Components and Techniques*, edited by K. J. Button (Academic, New York, 1985), pp. 123–171.

[18] R. J. Wylde, IEE Proc. **131-H**, 258 (1984).

[19] J. A. Murphy, Int. J. Infrared Millimeter Waves **8**, 1165 (1987).

[20] R. K. Garg and M. M. Pradhan, Infrared Phys. **18**, 292 (1978).

[21] H. Kogelnik, Appl. Opt. **4**, 1562 (1965).

[22] J. R. Birch, J. D. Dromey, and J. Lesurf, Infrared Phys. **21**, 225 (1981).

[23] A. F. Harvey, *Microwave Engineering* (Academic, New York, 1963), pp. 44–45.

[24] D. Boucher, J. Burie, R. Bocquet, and W. Chen, Int. J. Infrared Millimeter Waves **13**, 1395 (1992).

[25] E. M. T. Jones and S. B. Cohn, J. Appl. Phys. **26**, 452 (1955).

[26] A. E. Costley, K. H. Hursey, C. F. Neill, and J. M. Ward, J. Opt. Soc. Am. **67**, 979 (1977).

[27] D. A. Bathker, IEEE Trans. Microwave Theory Tech. **MTT-15**, 128 (1967).

[28] G. D. Holah, in *Infrared and Millimeter Waves: Systems and Components*, edited by K. J. Button (Academic, New York, 1982), Chap. 6.

[29] R. Ulrich, Infrared Phys. **7**, 37 (1967).

[30] M. L. Khidekel and E. I. Zhilyaeva, Synth. Met. **4**, 1 (1981).

[31] C. P. Slichter, *Principles of Magnetic Resonance*, 3rd ed. (Springer, Berlin, 1989).

[32] J. P. Barnes, K. A. Earle, and J. H. Freed (unpublished results).

[33] M. V. Schneider, in *Infrared and Millimeter Waves: Systems and Components*, edited by K. J. Button (Academic, New York, 1982), Vol. 6, Chap. 4.

[34] N. R. Erickson, Int. J. Infrared Millimeter Waves **8**, 1015 (1987).